PHYSICAL REVIEW A **102**, 043313 (2020)

Synthetic Hall tube of interacting fermions

Xiaofan Zhou,[1] Gang Chen,[1,2,3,*] and Suotang Jia[1,2]
[1] *State Key Laboratory of Quantum Optics and Quantum Optics Devices, Institute of Laser Spectroscopy, Shanxi University, Taiyuan 030006, China*
[2] *Collaborative Innovation Center of Extreme Optics, Shanxi University, Taiyuan, Shanxi 030006, China*
[3] *Collaborative Innovation Center of Light Manipulations and Applications, Shandong Normal University, Jinan 250358, China*

(Received 9 August 2020; accepted 22 September 2020; published 9 October 2020)

Motivated by a recent experiment [J. H. Han *et al.*, Phys. Rev. Lett. **122**, 065303 (2019)], we investigate the many-body physics of interacting fermions in a synthetic Hall tube, using a state-of-the-art density-matrix renormalization-group numerical method. Since the interleg couplings of this synthetic Hall tube generate an interesting spin-tensor Zeeman field, exotic topological and magnetic properties occur. In particular, four quantum phases, such as nontopological spin-vector and -tensor paramagnetic insulators, and topological and nontopological spin-mixed paramagnetic insulators, are predicted by calculating the entanglement spectrum, entanglement entropies, energy gaps, and local magnetic orders with three spin vectors and five spin tensors. Moreover, the topologically magnetic phase transitions induced by the interaction as well as the interleg couplings are also revealed. Our results establish a way to explore many-body (topological) states induced by both the spiral spin-vector and -tensor Zeeman fields.

DOI: 10.1103/PhysRevA.102.043313

I. INTRODUCTION

Since the discovery of the quantum Hall effect [1], the exploration of novel topological states of matter has attracted a great deal of attention both theoretically and experimentally, since they provide important applications in designing novel quantum devices and processing quantum information. The Hofstadter-Harper Hamiltonian is one of the fundamental models that are used to investigate topological states [2]. The experimental realization of such a Hamiltonian in cold atomic gases creates the opportunity for simulating topological states [3–5]. In cold-atom systems, the internal degrees of freedom of atoms, such as the hyperfine spins and clock states [6–14], can be treated as a synthetic dimension to simulate the $(D+1)$-dimensional quantum physics using D-dimensional lattices [15], e.g., the four-dimensional quantum Hall effect [16] and chiral edge current of Hall ribbons [6,7].

Using three hyperfine states as a synthetic lattice dimension and coupling them through synthetic gauge fields by the two-photon Raman process [17], spin-1 spin-orbit coupling [18–22] and spin-tensor-momentum coupling [23,24] have also been implemented. When the links between the hyperfine states are cyclical with a gauge flux $\phi = 2\pi/3$, the optical lattice can form a synthetic Hall tube [25,26], which is a simple Hofstadter-Harper Hamiltonian [2]. The synthetic Hall tube supports a generalized inversion symmetry-protected topological insulator [27], which is similar to the integer quantum Hall state. Since the time-reversal, particle-hole, and chiral symmetries are broken, this topological insulator belongs to the symmetry class A (unitary) of the Altland-Zirnbauer classification [28–31]. By varying one of the interleg coupling strengths, there exists a topological phase transition with a closing band gap at the critical point [25]. In a recent experiment, this interesting synthetic Hall tube was realized successfully in the alkaline-earth fermions [32].

Apart from the single-particle quantum regulation in cold-atom experiments, the interactions between the internal states can be controlled via Feshbach resonances [33] and more importantly generate rich many-body phenomena [34–40]. However, the interacting synthetic Hall tube has not been fully investigated. In this paper we investigate many-body properties of such a system, based on a state-of-the-art density-matrix renormalization-group (DMRG) numerical method [41,42]. Since the interleg couplings of this synthetic Hall tube generate an interesting spin-tensor Zeeman field, it is necessary to explore magnetic properties of the system, apart from the interaction-driven topological transition. Due to the coexistence of the spiral spin-vector and -tensor Zeeman fields in the synthetic Hall tube, local magnetic orders with three spin vectors and five spin tensors should be introduced [43]. In terms of the calculated entanglement spectrum, entanglement entropies, energy gaps, and local magnetic orders, we find four quantum phases such as nontopological spin-vector and -tensor paramagnetic insulators, and topological and nontopological spin-mixed paramagnetic insulators. Moreover, the topologically magnetic phase transitions induced by the interaction as well as the interleg couplings are also revealed. Our results provide a way to explore many-body (topological) states induced by both the spiral spin-vector and -tensor Zeeman fields.

II. MODEL AND HAMILTONIAN

Similarly to Ref. [32], here we consider the alkaline-earth fermions ^{173}Yb trapped in an effective one-dimensional

---

[*] chengang971@163.com

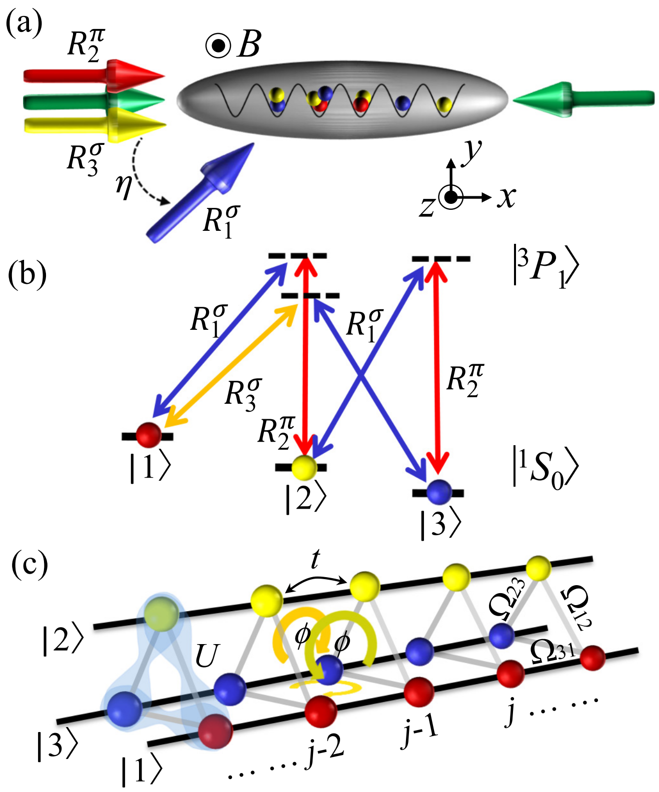

FIG. 1. (a) Schematics of the system setup with three Raman lasers $R_{1,2,3}^{\sigma,\pi,\sigma}$, which are represented by the yellow, blue, and red arrows, respectively. Here R_1^σ has is at an angle η from the x axis. A magnetic field B along the z axis is applied to lift the spin degeneracy of the ground state $|^1S_0\rangle$. (b) Three hyperfine spin states in the ground state $|^1S_0\rangle$ of alkaline-earth(-like) atoms ^{173}Yb are coupled by three two-photon Raman transitions. (c) Synthetic Hall tube with a uniform flux ϕ on each side plaquette and interaction U between these hyperfine spin states.

optical lattice (in the x direction), where the system is highly confined in the other two directions (y and z) and takes a cigar-shaped structure (i.e., tube), as shown in Fig. 1(a). Three hyperfine spin states of the ground state $|^1S_0\rangle$, i.e., $|1\rangle = |F = 5/2, m_F = -5/2\rangle$, $|2\rangle = |F = 5/2, m_F = -3/2\rangle$, and $|3\rangle = |F = 5/2, m_F = -1/2\rangle$, are chosen as three legs, as shown in Fig. 1(b). Three linearly polarized Raman laser beams $R_{1,2,3}^{\sigma,\pi,\sigma}$ are used to make three two-photon Raman transitions between the states $|^1S_0, F = 5/2\rangle$ and $|^3P_1, F = 7/2\rangle$. The couplings $|1\rangle \leftrightarrow |2\rangle$ and $|2\rangle \leftrightarrow |3\rangle$ are the π-σ transitions ($\Delta m_F = 1$), while the coupling $|1\rangle \leftrightarrow |3\rangle$ is the σ-σ transition ($\Delta m_F = 2$), as shown in Fig. 1(b). Thus, the three-component atomic tunneling along the lattice and three-leg couplings with a complex phase factor form a synthetic tube with a uniform flux per plaquette, as shown in Fig. 1(c).

When the effective one-dimensional optical lattice is deep enough and the Rabi frequency of the two-photon Raman transitions is not too large, we use the single-band approximation to derive the tight-binding model Hamiltonian [32]

$$\hat{H} = \hat{H}_{\mathrm{hop}} + \hat{H}_{\Omega} + \hat{H}_{\mathrm{int}}, \tag{1}$$

where the tunneling Hamiltonian

$$\hat{H}_{\mathrm{hop}} = \sum_{j,\sigma}(-t\hat{c}_{j+1,\sigma}^{\dagger}\hat{c}_{j,\sigma} + \mathrm{H.c.}), \tag{2}$$

the interleg coupling Hamiltonian

$$\hat{H}_{\Omega} = \frac{1}{2}\sum_{j,\sigma\neq\sigma'}(\Omega_{\sigma\sigma'}e^{i\phi j}\hat{c}_{j,\sigma}^{\dagger}\hat{c}_{j,\sigma'} + \mathrm{H.c.}), \tag{3}$$

and the interaction Hamiltonian

$$\hat{H}_{\mathrm{int}} = U\sum_{j,\sigma\neq\sigma'}\hat{n}_{j,\sigma}\hat{n}_{j,\sigma'}. \tag{4}$$

Along the real space, the interaction is on site and short ranged, while in the synthetic dimension, the interaction is long ranged. In Eqs. (2) and (3), $\hat{c}_{j,\sigma}$ ($\hat{c}_{j,\sigma}^{\dagger}$) is the annihilation (creation) operator for a fermion at the real lattice site $j = 1, \dots, L$ with spin $\sigma = (1, 2, 3)$ and the lattice length L. In Eq. (4) $\hat{n}_{j,\sigma} \equiv \hat{c}_{j,\sigma}^{\dagger}\hat{c}_{j,\sigma}$ is the number operator. In addition, t is the tunneling rate; $\Omega_{\sigma\sigma'}$ is the Rabi frequency of the two-photon Raman transition between the spin states $|\sigma\rangle$ and $|\sigma'\rangle$ and is set to $\Omega_{12} = \Omega_{23}$ for simplicity; the j-dependent complex phase factor $e^{i\phi j}$ results from the momentum imparted by the two-photon Raman transitions; the flux $\phi = k_R d_x(1 - \cos\eta)$, with k_R the recoil momentum of the Raman lasers and d_x the lattice constant; U is the interaction strength, and H.c. is the Hermitian conjugate.

The Hamiltonian (1) has a distinct advantage that all parameters can be tuned independently. For example, t can be tuned by varying the depth of the optical lattice, $\Omega_{\sigma\sigma'}$ can be controlled by adjusting the magnitudes of the Raman laser beams, ϕ can be manipulated by controlling the angle η, and U can be tuned via the external magnetic field through an orbital Feshbach resonance [44–46] or via the transverse trapping frequencies through the confinement-induced resonance [47,48]. In the following, we mainly consider the case of the unit filling, i.e., $n = N/L = 1$, with N the total number of atoms, and $\phi = 2\pi/3$, since the system exhibits a synthetic Hall tube in such a condition. We also address the repulsive interaction $U > 0$ and set $t = 1$ as a unit.

In the absence of interaction ($U = 0$), when $\Omega_- < \Omega_{31} < \Omega_+$ with $\Omega_\pm = \pm 3t + \sqrt{\Omega_{12}^2 + 9t^2}$, this synthetic Hall tube supports a topological insulator protected by generalized inversion symmetry [25,27,32]. Since the time-reversal, particle-hole, and chiral symmetries are broken, the topological insulator belongs to the unitary symmetry class A (unitary) of the Altland-Zirnbauer classification and is characterized by a $\mathbb{Z}$ invariant [28–31]. More interestingly, the interleg couplings generate spatially periodic spin-vector and -tensor Zeeman fields with the Hamiltonian

$$\hat{H}_{\Omega} = \sum_j \Omega_{12}\big[\cos(\phi j)S_j^x - \sin(\phi j)S_j^y\big] + \Omega_{31}\big[\cos(\phi j)\big(N_j^{xx} - N_j^{yy}\big) + \sin(\phi j)N_j^{xy}\big], \tag{5}$$

where $\mathbf{S}_j = \sum_{\sigma\sigma'} b_{j\sigma}^{\dagger}\mathbf{F}_{\sigma\sigma'}b_{j\sigma'}$, with $\mathbf{F}_{\sigma\sigma'}$ the spin operators of the total angular momentum $F = 1$; $N^{\alpha\beta} = \{S^\alpha, S^\beta\}/2 - \delta_{\alpha\beta}\mathbf{S}^2/3$ is the anticommutation relation with $\alpha(\beta) = (x, y, z)$; Ω_{12} and Ω_{31} are called the spin-vector and -tensor Zeeman fields, respectively; and $2\pi/\phi$ is the spiral period of the Zeeman field. When $\Omega_{31} = 0$, the synthetic Hall tube reduces to the spin-1 spin-orbit-coupled optical lattice only with the spin-vector Zeeman field [18–21], which has a trivial topology. Notice that Ω_{12} can also be treated as the spin-tensor Zeeman field since the Hamiltonian (5) has rotational symmetry.

In the presence of weak interaction, the topological insulator with the $\mathbb{Z}$ invariant still exists since the generalized inversion symmetry remains [49]. By further increasing the interaction strength, the topology of the system becomes trivial. On the other hand, the interaction Hamiltonian (4) can also be rewritten in a magnetic form

$$\hat{H}_{\rm int} = \frac{U}{2}\sum_j S_j^{z2}(\hat{n}_j - 1). \tag{6}$$

This shows clearly that at half filling ($n = 1$), the interaction contributes little to the magnetism of the system, i.e., the magnetic properties of the synthetic Hall tube are mainly determined by $\hat{H}_\Omega$.

Based on the above qualitative analysis, it can be found that the synthetic Hall tube exhibits exotic topological and magnetic properties arising from the competition between the tunneling, spin-vector and -tensor Zeeman fields, and interactions. In order to quantitatively reveal them, we will use a state-of-the-art DMRG numerical method, for which we retain 400 truncated states per DMRG block and perform 30 sweeps with a maximum truncation error on the order of 10^{-10}.

III. ORDER PARAMETERS

The many-body topological properties can be well described by the degeneracy in the entanglement spectrum, entanglement entropy, chemical potential spectrum, and excited energy gap. The entanglement spectrum is defined as [50]

$$\xi_i = -\ln(\rho_i), \tag{7}$$

where ρ_i is the eigenvalue of the reduced density matrix $\hat{\rho}_A = {\rm Tr}_B|\psi\rangle\langle\psi|$, with $|\psi\rangle$ the ground-state wave function and A and B corresponding to the left and the right half of the one-dimensional chain, respectively. The system is topological if the entanglement spectrum is degenerate since the entanglement spectrum resembles the energy spectrum of edge excitations and vice versa [50–56]. The quantum criticality of the interaction-driven topological phase transition can be governed by the von Neumann entropy [56–61]

$$S_{\rm vN} = -{\rm Tr}_A(\hat{\rho}_A \log\hat{\rho}_A). \tag{8}$$

The divergence of the von Neumann entropy at the critical point not only indicates a continuous transition but also yields a central charge, which reflects the universality class of phase transition. The von Neumann entropy of a subchain of length l is given by

$$S_{\rm vN} = \frac{C}{6}\ln\left(\sin\frac{\pi l}{L}\right) + {\rm const}, \tag{9}$$

in which the slope at a large distance gives the central charge C of the conformal field theory underlying the critical behavior [62,63].

The appearance of edge states is usually considered to be a hallmark of topological properties for the bulk system. The topological insulator of the synthetic Hall tube has two gapless edge states inside the gap between the lowest and the upper branches in the chemical potential spectrum [25], which is essentially the energy required to add an atom to a system of N atoms and can be defined as

$$\mu = E_g^o(N) - E_g^o(N-1). \tag{10}$$

Here $E_g^o(N)$ is the ground-state energy of N atoms under open boundary conditions. The topological ground state of the synthetic Hall tube is nondegenerate and separated from the first excited state by a finite gap, which closes and reopens in the process of the topological phase transition [32]. The excited energy gap is defined as

$$\Delta_e = E_e^p(N) - E_g^p(N), \tag{11}$$

where $E_e^p(N)$ [$E_g^p(N)$] is the first-excited-state (ground-state) energy of N atoms under periodic boundary conditions.

Due to the coexistence of the spin-vector and -tensor Zeeman fields, the magnetism of the synthetic Hall tube should be described by whole spin-1 local magnetic orders (eight spin moments with three spin vectors and five spin tensors) and their correlations [43]. The local spin vector

$$\vec{S}_j = \left(\langle S_j^x\rangle, \langle S_j^y\rangle, \langle S_j^z\rangle\right)^T, \tag{12}$$

while the local spin-tensor fluctuation matrix T_j has tensor moments

$$T_j^{\alpha\beta} = \langle\{S_j^\alpha, S_j^\beta\}\rangle/2 - \langle S_j^\alpha\rangle\langle S_j^\beta\rangle. \tag{13}$$

Geometrically, $\vec{S}_j$ is characterized by an arrow and T_j is governed by an ellipsoid [with principle axis lengths $l_T^n(j)$ ($n = a, b, c$) and orientations $\vec{v}_T^n(j)$ given by the square roots of the eigenvalues and eigenvectors of $T_j^{\alpha\beta}$ [64]]. Since the magnetic properties are mainly determined by $\hat{H}_\Omega$, all the insulators are spiral paramagnetic phases without any long-range correlations. As a result, eight independent geometric parameters, including the length l_S and spherical coordinates θ_S and ϕ_S of the arrow, the two axis lengths $l_T^{a,b}$ with the third axis length $l_T^c = \sqrt{2-(l_S)^2-(l_T^a)^2-(l_T^b)^2}$, and the orientational Euler angles θ_T, ϕ_T, and ϕ_T' of the ellipsoid, are chosen to quantitatively characterize and geometrically visualize the magnetic orders.

IV. QUANTUM PHASES

A. Noninteracting case ($U = 0$)

We first address the case of the noninteracting case ($U = 0$). For $\Omega_- < \Omega_{31} < \Omega_+$, the ground state is a topological insulator and vice versa. As a result, we can discuss the magnetisms of the topological and nontopological insulators as varying the spin-tensor Zeeman field Ω_{31} for a fixed spin-vector Zeeman field $\Omega_{12}/t = 12.3$. When $\Omega_{31} = 0$, the system is the same as the spin-1 spin-orbit-coupled optical lattice only with the spin-vector Zeeman field [18–21]. In this case, the spin-vector arrow has a unit length $l_S = 1$ and spirals in the x-y plane (i.e., θ_S is a constant and ϕ_S changes cyclically), as shown in Figs. 2(a i) and 2(a ii). The spin-tensor ellipsoid almost

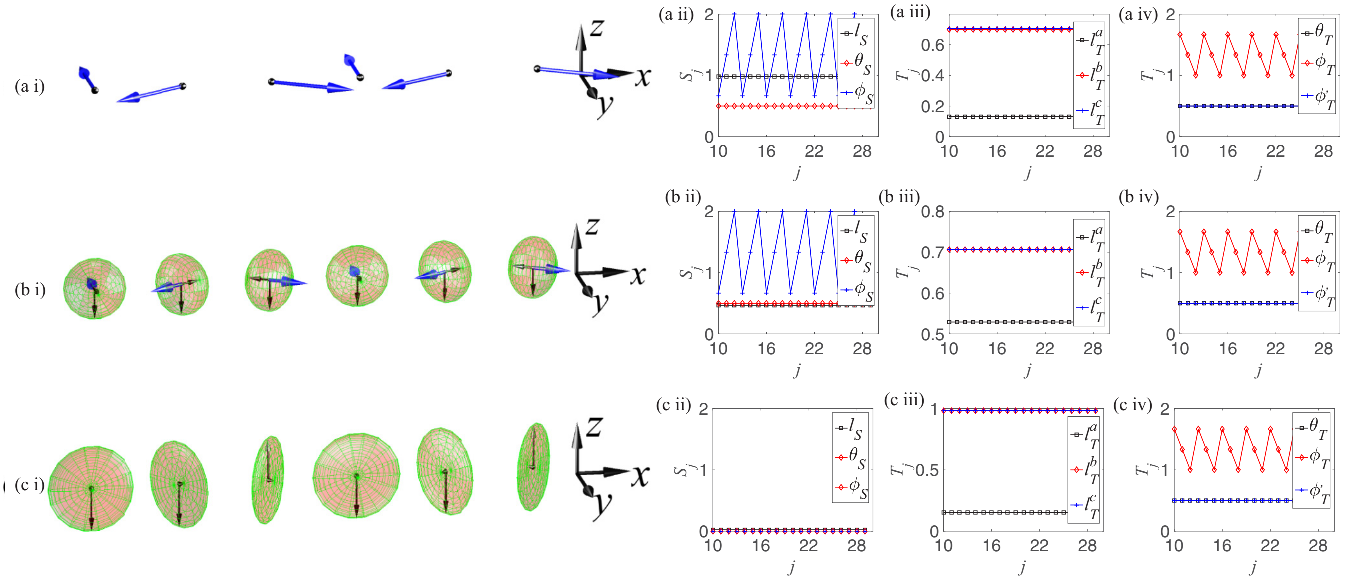

FIG. 2. (a i), (b i), and (c i) Schematic diagrams of the spin-vector density arrows $\vec{S}_j$ and the spin-tensor density ellipsoids T_j. The blue arrow denotes the spin vector $\vec{S}$, while the red ellipsoid reflects the spin tensor T, in which the black arrows are the ellipsoid's axis orientations. (a ii), (b ii), and (c ii) Spatial distributions of $[l_S(j), \theta_S(j), \phi_S(j)]$ for the vector-density arrows $\vec{S}_j$. (a iii), (b iii), and (c iii) Distributions of the axis lengths $l_T^n(j)$ $(n = a, b, c)$ of the spin-tensor density ellipsoids T_j. (a iv), (b iv), and (c iv) Distributions of the orientational Euler angles θ_T, ϕ_T, and ϕ'_T of the spin-tensor density ellipsoids T_j. The parameters are $\Omega_{12}/t = 12.3$, $U/t = 0$, $L = 64$, and (a) $\Omega_{31}/t = 0$, (b) $\Omega_{31}/t = 12.3$, and (c) $\Omega_{31}/t = 19$.

is a plate with large $l_T^{b,c}$ and small l_T^a [see Fig. 2(a iii)] and also spirals with a cyclical variation ϕ_T and constants θ_T and ϕ'_T [see Fig. 2(a iv)], since the spin-tensor ellipsoid depends crucially on the three spin-vector operators S^α [see Eq. (13)]. This paramagnetic insulator dominated only by the spin vector is called nontopological spin-vector paramagnetic insulator (NTSV). For $\Omega_{31} < \Omega_-$ (i.e., a small spin-tensor Zeeman field), the ground state is still the NTSV.

For the topological regime with $\Omega_- < \Omega_{31} < \Omega_+$, the spin-vector arrows also spiral in the x-y plane but have short lengths $l_S < 1$, as shown in Figs. 2(b i) and 2(b ii). In this case, the spin vector cannot fully describe the magnetic properties and the spin tensor should be considered. The spin-tensor ellipsoids have finite $l_T^{a,b,c}$ [see Fig. 2(b iii)] and also spiral in the x-y plane with a cyclical variation ϕ_T and constants θ_T and ϕ'_T [see Fig. 2(b iv)]. Different from the NTSV, this spiral spin-tensor ellipsoid only depends on the spin-tensor Zeeman field. This topological insulator is called a topological spin-mixed paramagnetic insulator (TSM). For $\Omega_{31} > \Omega_+$ (i.e., a large spin-tensor Zeeman field), the spin-vector arrow vanishes (i.e., $l_S = 0$), as shown in Figs. 2(c i) and 2(c ii). In this case, the magnetic orders are fully dominated by the spin-tensor ellipsoid. The ellipsoids have $l_T^{b,c} \sim 1$ and $l_T^a \to 0$ [see Fig. 2(c iii)] and also spiral in the x-y plane with a cyclical variation ϕ_T and constants θ_T and ϕ'_T [see Fig. 2(c iv)]. This paramagnetic insulator without the spin vector is called a nontopological spin-tensor paramagnetic insulator (NTST).

The above analysis of Fig. 2 shows that there exist two topologically magnetic phase transitions with increasing spin-tensor Zeeman field Ω_{31}/t. One is the transition from the NTSV to the TSM at $\Omega_{31}^{c1} = \Omega_-$. At this critical point, the spin-vector arrow length l_S drops rapidly, but the ellipsoid's axis lengths $l_T^{a,b,c}$ increase rapidly [see Fig. 3(a)]. The other is the transition from the TSM to the NTST at $\Omega_{31}^{c2} = \Omega_+$. At this critical point, the spin-vector arrow length l_S suddenly becomes zero and the ellipsoid's axis lengths $l_T^{a,b}$ (l_T^c) increase (decrease) abruptly [see Fig. 3(a)]. The derivatives of the lengths are not continuous at the critical points $\Omega_{31}^{c1,c2}$ [see Fig. 3(b)]. Figure 3(c) shows the phase diagram in the Ω_{31}-Ω_{12} plane. Both the phase transitions of NTSV ↔ TSM and TSM ↔ NTST [see blue lines in Fig. 3(c)] are of second order with a closing excited energy gap Δ_e at the critical points [25,32].

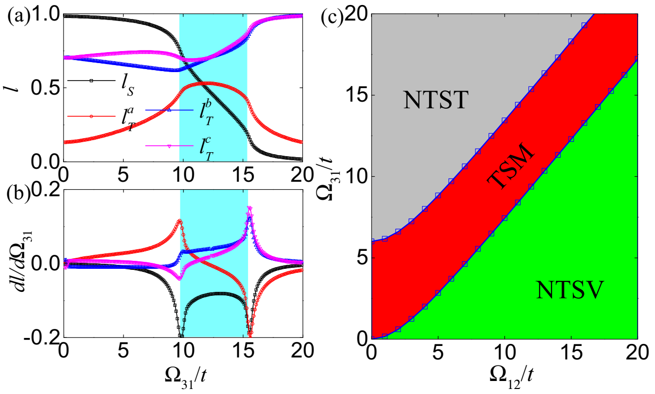

FIG. 3. (a) Lengths and (b) derivatives of the spin-vector arrow l_S and the axis lengths of the spin-tensor ellipsoid $l_T^{a,b,c}$ as functions of the spin-tensor Zeeman field Ω_{31}/t with a spin-vector Zeeman field $\Omega_{12}/t = 12.3$. (c) Phase diagram in the Ω_{12}-Ω_{31} plane. In all panels $U = 0$ and $L = 64$.

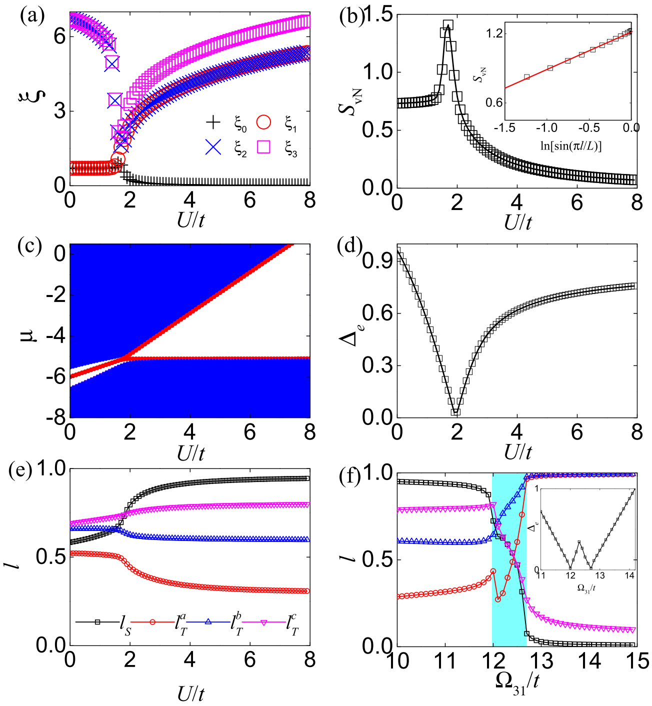

FIG. 4. (a) Four lowest levels in the entanglement spectrum ξ_i ($i = 0, 1, 2, 3$), (b) von Neumann entropy S_{vN}, (c) chemical potential spectrum μ, (d) excited energy gap Δ_e, and (e) length of the spin-vector arrow l_S and axis lengths of the spin-tensor ellipsoid $l_T^{a,b,c}$ as functions of the interaction strength U/t. In (a)–(c) and (e), $\Omega_{31}/t = 11$ and $L = 32$ and the open boundary condition is used. In (d), $\Omega_{31}/t = 11$ and $L = 12$ and the periodic boundary condition is used. The inset in (b) shows the von Neumann entropy of a subchain of length l as a function of $\sin(\pi l/N)$ for a chain with $L = 32$ at the critical point $U_c/t = 1.85$. The solid line is the linear fit $S_{\mathrm{vN}} = \frac{C}{6}\ln[\sin(\pi l/N)] + 1.22$ with $C \approx 2$. The central charge is six times the slope of the linear fit. (f) Length of the spin-vector arrow l_S and axis lengths of the spin-tensor ellipsoid $l_T^{a,b,c}$, as well as the excited energy gap Δ_e in the inset, as functions of the spin-tensor Zeeman field Ω_{31}/t with the interaction strength $U/t = 6$. In (f), $L = 32$ and the open boundary condition is used. In the inset of (f), $L = 12$ and the periodic boundary condition is used. In all panels $\Omega_{12}/t = 12.3$.

B. Interacting case ($U > 0$)

We now explore many-body properties induced by the repulsive interaction ($U > 0$). We first address the topological properties driven by the interaction, when $\Omega_{12}/t = 12.3$ and $\Omega_{31}/t = 11$. For a weak interaction, the entanglement spectrum ξ_i is twofold degeneracy and no longer degenerate beyond a critical interaction strength $U_c/t \sim 1.85$, as shown in Fig. 4(a). Without any symmetry breaking in this processing, it is a typical topological phase transition from a topological insulator to a nontopological insulator. As demonstrated in Fig. 4(b), sharp features of the von Neumann entropy S_{vN} emerge at the critical point. From the inset in Fig. 4(b), we estimate $C \sim 1.97$, which is close to the universality class of the Luttinger liquid ($C = 2$) and shows the continuity of the topological phase transition. On the other hand, in the absence of interaction, there are two gapless edge states inside the bulk band gap in the chemical potential spectrum μ. By increasing the interaction strength beyond a critical value U_c/t, these edge states merge into the bulk band and the system becomes a nontopological insulator, as shown in Fig. 4(c). Moreover, the excited energy gap Δ_e closes at the same critical value and then reopens, as shown in Fig. 4(d). This critical point is consistent with that derived from entanglements in Figs. 4(a) and 4(b).

We now explore the magnetic orders in the presence of interaction. Based on the above graphics of Fig. 2, it can be found that the spin-vector arrows and the spin-tensor ellipsoids exhibit the same spiral features, but show the distinct lengths l_S and $l_T^{a,b,c}$. This means that these lengths are adequate to describe the magnetic properties. As a result, we only calculate the lengths l_S and $l_T^{a,b,c}$ and ignore the angles θ_S, ϕ_S, θ_T, ϕ_T, and ϕ_T' hereafter.

In Fig. 4(e) we plot the lengths l_S and $l_T^{a,b,c}$ as functions of the interaction strength U/t. This figure shows that at the critical point U_c/t, the spin-vector arrow length l_S suddenly increases to $l_S \sim 1$ and the spin-tensor ellipsoid's axis lengths $l_T^{a,b}$ drop rapidly, which indicates that this topologically magnetic phase transition from the TSM to the NTSV occurs. In Fig. 4(f) we plot the lengths l_S and $l_T^{a,b,c}$ as functions of the spin-tensor Zeeman field strength Ω_{31} for a large interaction strength $U/t = 6$. In this case, all the insulators are nontopological since the entanglement spectrum ξ_i is nondegenerate. Interestingly, with increasing spin-tensor Zeeman field Ω_{31}, the vector length l_S and the ellipsoid's axis lengths $l_T^{a,b}$ first remain the same and then l_S rapidly decreases to $l_S < 1$ and $l_T^{a,b}$ (l_T^c) increase (decreases) rapidly. The corresponding phase is called the nontopological spin-mixed paramagnetic insulator (NTSM). Further increasing the spin-tensor Zeeman field Ω_{31}, l_S suddenly drops to $l_S \sim 0$ and $l_T^{a,b}$ rapidly increase to $l_T^{a,b} \sim 1$, i.e., the system enters into the NTST. In the processing of the nontopological magnetic phase transition, the excited energy gap Δ_e also closes at the critical points, as shown in inset of Fig. 4(f). Note that for a small interaction, the fundamental properties are similar to those in Fig. 3(a) and thus not plotted here. We also calculate the orders of other

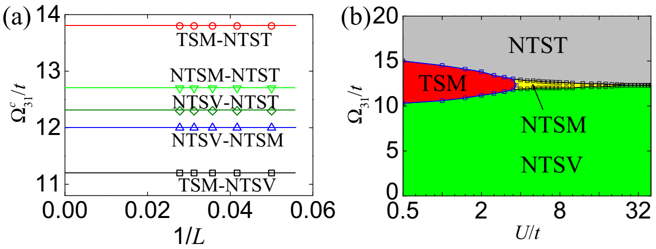

FIG. 5. (a) Finite-size scaling of the critical points Ω_{31}^c/t of the TSM-NTST transition (red circles) with $U/t = 2$, the TSM-NTSV transition (black squares) with $U/t = 2$, the NTSM-NTST transition (green down triangles) with $U/t = 6$, the NTSV-NTSM transition (blue up triangles) with $U/t = 6$, and the NTSV-NTST transition (olive diamonds) with $U/t = 32$. The symbols are the DMRG results and the solid lines are the fitting. (b) Phase diagram in the Ω_{31}-U plane for the spin-vector Zeeman field $\Omega_{12}/t = 12.3$. The blue and black lines show the continuous phase transitions. The blue lines denote the liquids with $C = 2$.

finite-sizes systems and find that the orders have the same features. By using finite-size scaling, we get the critical points of phase transitions in the thermodynamic limits, which are almost the same as those of finite-size systems, as shown in Fig. 5(a).

Finally, with the help of the calculated entanglement spectrum, entanglement entropies, energy gaps, and local magnetic orders, in Fig. 5(b) we map out the phase diagram in the Ω_{31}-U plane for the spin-vector Zeeman field $\Omega_{12}/t = 12.3$. This figure shows clearly four different phases such as the TSM, the NTSM, the NTSV, and the NTST, which are well controlled by both the spin-vector and -tensor Zeeman fields as well as the repulsive interaction. The NTSM phase shrinks between the NTSV and NTST phases and finally disappears when increasing the interaction strength U. Moreover, all the phase transitions with a closing excited energy gap Δ_e are of second order.

V. CONCLUSION

Before concluding this paper, we briefly discuss how to observe these quantum phases and phase transitions in cold-atom experiments. The entanglement entropy can be measured using quantum interference of many-body twins of ultracold atoms in optical lattices [61]. The excited energy gap closing in the processing of the topological phase transition can be observed via momentum-resolved analysis of the quench dynamics [32]. The local magnetic orders can be measured by isolating the sites of interest using additional site-resolved potentials [65–68]. Thus, all the quantum phases and phase transitions can be observed in current experimental setups.

In conclusion, we have studied the many-body physics of an interacting synthetic Hall tube by the state-of-the-art DMRG numerical method. We have found four quantum phases, including the TSM, the NTSM, the NTSV, and the NTST, by means of the calculated entanglement spectrum, entanglement entropies, energy gaps, and local magnetic orders. These quantum phases depend crucially on the interaction and the spiral spin-vector and -tensor Zeeman fields induced by the interleg couplings. Our work provides a way to explore many-body (topological) states induced by both the spiral spin-vector and -tensor Zeeman fields.

ACKNOWLEDGMENTS

This work was supported by the National Key R&D Program of China under Grant No. 2017YFA0304203; the NSFC under Grants No. 11674200, No. 12074232, and No. 12004230; the Fund for Shanxi "1331 Project" Key Subjects Construction; and Research Project Supported by Shanxi Scholarship Council of China.

[1] K. v. Klitzing, G. Dorda, and M. Pepper, New Method for High-Accuracy Determination of the Fine-Structure Constant Based on Quantized Hall Resistance, Phys. Rev. Lett. **45**, 494 (1980).

[2] D. R. Hofstadter, Energy levels and wave functions of Bloch electrons in rational and irrational magnetic fields, Phys. Rev. B **14**, 2239 (1976).

[3] N. Goldman, J. C. Budich, and P. Zoller, Topological quantum matter with ultracold gases in optical lattices, Nat. Phys. **12**, 639 (2016).

[4] M. E. Tai, A. Lukin, M. Rispoli, R. Schittko, T. Menke, D. Borgnia, P. M. Preiss, F. Grusdt, A. M. Kaufman, and M. Greiner, Microscopy of the interacting Harper-Hofstadter model in the two-body limit, Nature (London) **546**, 519 (2017).

[5] N. R. Cooper, J. Dalibard, and I. B. Spielman, Topological bands for ultracold atoms, Rev. Mod. Phys. **91**, 015005 (2019).

[6] M. Mancini, G. Pagano, G. Cappellini, L. Livi, M. Rider, J. Catani, C. Sias, P. Zoller, M. Inguscio, M. Dalmonte, and L. Fallani, Observation of chiral edge states with neutral fermions in synthetic Hall ribbons, Science **349**, 1510 (2015).

[7] B. K. Stuhl, H.-I. Lu, L. M. Aycock, D. Genkina, and I. B. Spielman, Visualizing edge states with an atomic Bose gas in the quantum Hall regime, Science **349**, 1514 (2015).

[8] L. F. Livi, G. Cappellini, M. Diem, L. Franchi, C. Clivati, M. Frittelli, F. Levi, D. Calonico, J. Catani, M. Inguscio, and L. Fallani, Synthetic Dimensions and Spin-Orbit Coupling with an Optical Clock Transition, Phys. Rev. Lett. **117**, 220401 (2016).

[9] X. Zhou, J.-S. Pan, W. Yi, G. Chen, and S. Jia, Interaction-induced exotic vortex states in an optical lattice clock with spin-orbit coupling, Phys. Rev. A **96**, 023627 (2017).

[10] T. Y. Saito and S. Furukawa, Devil's staircases in synthetic dimensions and gauge fields, Phys. Rev. A **95**, 043613 (2017).

[11] L. D. Re and M. Capone, Selective insulators and anomalous responses in three-component fermionic gases with broken SU(3) symmetry, Phys. Rev. A **98**, 063628 (2018).

[12] C.-H. Li, Y. Yan, S. Choudhury, D. B. Blasing, Q. Zhou, and Y. P. Chen, A Bose-Einstein condensate on a synthetic Hall cylinder, arXiv:1809.02122.

[13] Y. Yan, S.-L. Zhang, S. Choudhury, and Q. Zhou, Emergent Periodic and Quasiperiodic Lattices on Surfaces of Synthetic Hall Tori and Synthetic Hall Cylinders, Phys. Rev. Lett. **123**, 260405 (2019).

[14] R. P. Anderson, D. Trypogeorgos, A. Valdés-Curiel, Q.-Y. Liang, J. Tao, M. Zhao, T. Andrijauskas, G. Juzeliunas, and I. B. Spielman, Realization of a deeply subwavelength adiabatic optical lattice, Phys. Rev. Research **2**, 013149 (2020).

[15] O. Boada, A. Celi, J. I. Latorre, and M. Lewenstein, Quantum Simulation of an Extra Dimension, Phys. Rev. Lett. **108**, 133001 (2012).

[16] H. M. Price, O. Zilberberg, T. Ozawa, I. Carusotto, and N. Goldman, Four-Dimensional Quantum Hall Effect with Ultracold Atoms, Phys. Rev. Lett. **115**, 195303 (2015).

[17] A. Celi, P. Massignan, J. Ruseckas, N. Goldman, I. B. Spielman, G. Juzeliūnas, and M. Lewenstein, Synthetic Gauge Fields in Synthetic Dimensions, Phys. Rev. Lett. **112**, 043001 (2014).

[18] S. S. Natu, X. Li, and W. S. Cole, Striped ferronematic ground states in a spin-orbit-coupled $S = 1$ Bose gas, Phys. Rev. A **91**, 023608 (2015).

[19] S. Barbarino, L. Taddia, D. Rossini, L. Mazza, and R. Fazio, Magnetic crystals and helical liquids in alkaline-earth fermionic gases, Nat. Commun. **6**, 8134 (2015).

[20] D. Campbell, R. Price, A. Putra, A. Valdés-Curiel, D. Trypogeorgos, and I. B. Spielman, Magnetic phases of spin-1 spin-orbit-coupled Bose gases, Nat. Commun. **7**, 10897 (2016).

[21] G. Martone, F. Pepe, P. Facchi, S. Pascazio, and S. Stringari, Tricriticalities and Quantum Phases in Spin-Orbit-Coupled Spin-1 Bose Gases, Phys. Rev. Lett. **117**, 125301 (2016).

[22] J. H. Pixley, W. S. Cole, I. B. Spielman, M. Rizzi, and S. D. Sarma, Strong-coupling phases of the spin-orbit-coupled spin-1 Bose-Hubbard chain: Odd-integer Mott lobes and helical magnetic phases, Phys. Rev. A **96**, 043622 (2017).

[23] X.-W. Luo, K. Sun, and C. Zhang, Spin-Tensor-Momentum-Coupled Bose-Einstein Condensates, Phys. Rev. Lett. **119**, 193001 (2017).

[24] D. Li, L. Huang, P. Peng, G. Bian, P. Wang, Z. Meng, L. Chen, and J. Zhang, Experimental realization of a spin-tensor momentum coupling in ultracold Fermi gases, Phys. Rev. A **102**, 013309 (2020).

[25] S. Barbarino, M. Dalmonte, R. Fazio, and G. E. Santoro, Topological phases in frustrated synthetic ladders with an odd number of legs, Phys. Rev. A **97**, 013634 (2018).

[26] X.-W. Luo, J. Zhang, and C. Zhang, Tunable flux through a synthetic Hall tube of neutral fermions, arXiv:2002.07617.

[27] H. L. Nourse, I. P. McCulloch, C. Janani, and B. J. Powell, Haldane insulator protected by reflection symmetry in the doped Hubbard model on the three-legged ladder, Phys. Rev. B **94**, 214418 (2016).

[28] C.-K. Chiu, J. C. Y. Teo, A. P. Schnyder, and S. Ryu, Classification of topological quantum matter with symmetries, Rev. Mod. Phys. **88**, 035005 (2016).

[29] A. Altland and M. R. Zirnbauer, Nonstandard symmetry classes in mesoscopic normal-superconducting hybrid structures, Phys. Rev. B **55**, 1142 (1997).

[30] A. P. Schnyder, S. Ryu, A. Furusaki, and A. W. W. Ludwig, Classification of topological insulators and superconductors in three spatial dimensions, Phys. Rev. B **78**, 195125 (2008).

[31] A. W. W. Ludwig, Topological phases: Classification of topological insulators and superconductors of non-interacting fermions, and beyond, Phys. Scr. **T168**, 014001 (2016).

[32] J. H. Han, J. H. Kang, and Y. Shin, Band Gap Closing in a Synthetic Hall Tube of Neutral Fermions, Phys. Rev. Lett. **122**, 065303 (2019).

[33] C. Chin, R. Grimm, P. Julienne, and E. Tiesinga, Feshbach resonances in ultracold gases, Rev. Mod. Phys. **82**, 1225 (2010).

[34] S. Raghu, X.-L. Qi, C. Honerkamp, and S.-C. Zhang, Topological Mott Insulators, Phys. Rev. Lett. **100**, 156401 (2008).

[35] I. Bloch, J. Dalibard, and W. Zwerger, Many-body physics with ultracold gases, Rev. Mod. Phys. **80**, 885 (2008).

[36] E. J. Mueller, Review of pseudogaps in strongly interacting Fermi gases, Rep. Prog. Phys. **80**, 104401 (2017).

[37] S. Rachel, Interacting topological insulators: A review, Rep. Prog. Phys. **81**, 116501 (2018).

[38] J. Jünemann, A. Piga, S.-J. Ran, M. Lewenstein, M. Rizzi, and A. Bermudez, Exploring Interacting Topological Insulators with Ultracold Atoms: The Synthetic Creutz-Hubbard Model, Phys. Rev. X **7**, 031057 (2017).

[39] X. Zhou, J.-S. Pan, Z.-X. Liu, W. Zhang, W. Yi, G. Chen, and S. Jia, Symmetry-Protected Topological States for Interacting Fermions in Alkaline-Earth-Like Atoms, Phys. Rev. Lett. **119**, 185701 (2017).

[40] S. de Léséleuc, V. Lienhard, P. Scholl, D. Barredo, S. Weber, N. Lang, H. P. Büchler, T. Lahaye, and A. Browaeys, Observation of a symmetry-protected topological phase of interacting bosons with Rydberg atoms, Science **365**, 775 (2019).

[41] S. R. White, Density Matrix Formulation for Quantum Renormalization Groups, Phys. Rev. Lett. **69**, 2863 (1992).

[42] U. Schollwök, The density-matrix renormalization group, Rev. Mod. Phys. **77**, 259 (2005).

[43] X. Zhou, X.-W. Luo, G. Chen, S. Jia, and C. Zhang, Quantum spiral spin-tensor magnetism, Phys. Rev. B **101**, 140412(R) (2020).

[44] R. Zhang, Y. Cheng, H. Zhai, and P. Zhang, Orbital Feshbach Resonance in Alkali-Earth Atoms, Phys. Rev. Lett. **115**, 135301 (2015).

[45] G. Pagano, M. Mancini, G. Cappellini, L. Livi, C. Sias, J. Catani, M. Inguscio, and L. Fallani, Strongly Interacting Gas of Two-Electron Fermions at an Orbital Feshbach Resonance, Phys. Rev. Lett. **115**, 265301 (2015).

[46] M. Höfer, L. Riegger, F. Scazza, C. Hofrichter, D. R. Fernandes, M. M. Parish, J. Levinsen, I. Bloch, and S. Fölling, Observation of an Orbital Interaction-Induced Feshbach Resonance in ^{173}Yb, Phys. Rev. Lett. **115**, 265302 (2015).

[47] R. Zhang, D. Zhang, Y. Cheng, W. Chen, P. Zhang, and H. Zhai, Kondo effect in alkaline-earth-metal atomic gases with confinement-induced resonances, Phys. Rev. A **93**, 043601 (2016).

[48] T. Bergeman, M. G. Moore, and M. Olshanii, Atom-Atom Scattering under Cylindrical Harmonic Confinement: Numerical and Analytic Studies of the Confinement Induced Resonance, Phys. Rev. Lett. **91**, 163201 (2003).

[49] T. Morimoto, A. Furusaki, and C. Mudry, Breakdown of the topological classification Z for gapped phases of noninteracting fermions by quartic interactions, Phys. Rev. B **92**, 125104 (2015).

[50] H. Li and F. D. M. Haldane, Entanglement Spectrum as a Generalization of Entanglement Entropy: Identification of Topological Order in Non-Abelian Fractional Quantum Hall Effect States, Phys. Rev. Lett. **101**, 010504 (2008).

[51] T. Yoshida, R. Peters, S. Fujimoto, and N. Kawakami, Characterization of a Topological Mott Insulator in One Dimension, Phys. Rev. Lett. **112**, 196404 (2014).

[52] J.-Z. Zhao, S.-J. Hu, and P. Zhang, Symmetry-Protected Topological Phase in a One-Dimensional Correlated Bosonic Model with a Synthetic Spin-Orbit Coupling, Phys. Rev. Lett. **115**, 195302 (2015).

[53] A. M. Turner, F. Pollmann, and E. Berg, Topological phases of one-dimensional fermions: An entanglement point of view, Phys. Rev. B **83**, 075102 (2011).

[54] F. Pollmann, A. M. Turner, E. Berg, and M. Oshikawa, Entanglement spectrum of a topological phase in one dimension, Phys. Rev. B **81**, 064439 (2010).

[55] L. Fidkowski, Entanglement Spectrum of Topological Insulators and Superconductors, Phys. Rev. Lett. **104**, 130502 (2010).

[56] S. T. Flammia, A. Hamma, T. L. Hughes, and X.-G. Wen, Topological Entanglement Rényi Entropy and Reduced Density Matrix Structure, Phys. Rev. Lett. **103**, 261601 (2009).

[57] M. B. Hastings, I. González, A. B. Kallin, and R. G. Melko, Measuring Rényi Entanglement Entropy in Quantum Monte Carlo Simulations, Phys. Rev. Lett. **104**, 157201 (2010).

[58] A. J. Daley, H. Pichler, J. Schachenmayer, and P. Zoller, Measuring Entanglement Growth in Quench Dynamics of Bosons in an Optical Lattice, Phys. Rev. Lett. **109**, 020505 (2012).

[59] D. A. Abanin and E. Demler, Measuring Entanglement Entropy of a Generic Many-Body System with a Quantum Switch, Phys. Rev. Lett. **109**, 020504 (2012).

[60] H.-C. Jiang, Z.-H. Wang, and L. Balents, Identifying topological order by entanglement entropy, Nat. Phys. **8**, 902 (2012).

[61] R. Islam, R. Ma, P. M. Preiss, M. E. Tai, A. Lukin, M. Rispoli, and M. Greiner, Measuring entanglement entropy in a quantum many-body system, Nature (London) **528**, 77 (2015).

[62] P. Calabrese and J. Cardy, Entanglement entropy and quantum field theory, J. Stat. Mech. (2004) 06002.

[63] A. E. B. Nielsen, G. Sierra, and J. I. Cirac, Violation of the area law and long-range correlations in infinite-dimensional-matrix product states, Phys. Rev. A **83**, 053807 (2011).

[64] H. M. Bharath, Non-Abelian geometric phases carried by the spin fluctuation tensor, J. Math. Phys. **59**, 062105 (2018).

[65] J. Simon, W. S. Bakr, R. Ma, M. E. Tai, P. M. Preiss, and M. Greiner, Quantum simulation of antiferromagnetic spin chains in an optical lattice, Nature (London) **472**, 307 (2011).

[66] M. F. Parsons, A. Mazurenko, C. S. Chiu, G. Ji, D. Greif, and M. Greiner, Site-resolved measurement of the spin-correlation function in the Fermi-Hubbard model, Science **353**, 1253 (2016).

[67] A. Mazurenko, C. S. Chiu, G. Ji, M. F. Parsons, M. Kanász-Nagy, R. Schmidt, F. Grusdt, E. Demler, D. Greif, and M. Greiner, A cold-atom Fermi-Hubbard antiferromagnet, Nature (London) **545**, 462 (2017).

[68] M. Boll, T. A. Hilker, G. Salomon, A. Omran, J. Nespolo, L. Pollet, I. Bloch, and C. Gross, Spin- and density-resolved microscopy of antiferromagnetic correlations in Fermi-Hubbard chains, Science **353**, 1257 (2016).